ACS OMEGA

http://pubs.acs.org/journal/acsodf

Article

Improved Permeability Model of the Binary Gas Interaction within a Two-Phase Flow and its Application in CO_2-Enhanced Coalbed Methane Recovery

Gang Wang, Feng Xu, Zhiyong Xiao,* Lu Zhang, Yujing Jiang, Feng Jiang, and Chengcheng Zheng

Cite This: *ACS Omega* 2022, 7, 31167−31182

Read Online

ACCESS | Metrics & More | Article Recommendations

ABSTRACT: In this paper, we develop a dual-porosity dual-permeability model for binary gas migration to explore the permeability evolution in the matrix and fracture in the process of a gas−water two-phase flow during CO_2-enhanced coalbed methane (CO_2-ECBM) recovery in coal reservoirs. This mechanistic model accommodates the effects of elastic deformation caused by the effective stress change in the matrix and fracture, the swelling/shrinkage deformation of the matrix caused by adsorption/desorption, the convection and diffusion of gas, and the discharge of water. Specifically, the time-dependent matrix swelling, from initially completely reducing the fracture aperture to finally affecting the coal bulk volume, is considered by the invaded volume fraction involving binary gas intrusion. The model is validated through laboratory data and applied to examine the permeability evolution of CO_2-ECBM recovery for 10 000 days. Furthermore, we analyze the sensitivity of some selected initial parameters to capture the key factors affecting CO_2-ECBM recovery. Our modeling results show that the permeability evolution can be divided into two stages during the process, where stage I is dominated by effective stress and stage II is dominated by adsorption/desorption. Increasing the injection pressure or initial permeability advances the start of stage II. The decrease in initial water saturation causes the permeability to change more drastically and the time of stage II to appear earlier until a time long enough, after which little effect is seen on the permeability results.

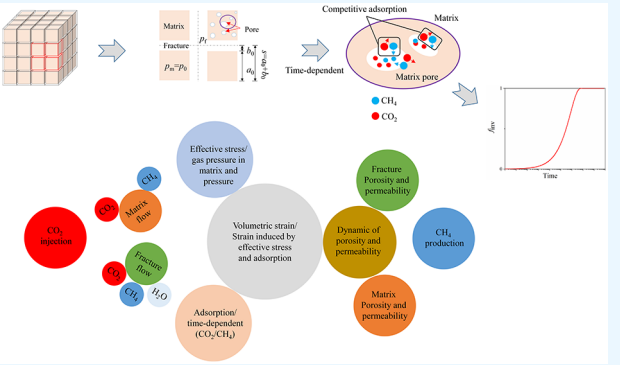

1. INTRODUCTION

Coalbed methane (CBM), extracted from coal seams as an alternative fuel to conventional energy sources such as coal, is emerging as a major contributor to an energy-hungry world.[1,2] With the increasing prominence of global warming, the goal of achieving "carbon emission peak" and "carbon neutrality" becomes increasingly urgent. The technology of injecting carbon dioxide into the deep unminable coal seams has attracted people's attention because it can effectively reduce greenhouse gases in the atmosphere and improve the production of coalbed methane and oil and gas recovery rates as well.[3,4] More and more laboratory tests and field tests have shown the potential and feasibility of carbon dioxide injection to produce CBM.[5−7] However, during the injection of CO_2 to enhance CBM, the permeability and porosity that primarily control the production of CBM will change dynamic due to the increase in gas pressure in the reservoir and the higher affinity of CO_2 to adsorb onto coal.[8] Furthermore, the consideration of the presence of water in the reservoir will complicate the fluid flow in CO_2-ECBM production.[9] Thus, establishing an accurate and comprehensive permeability model is crucial for CBM recovery and CO_2 geological storage.

Recently, a broad variety of works related to the mechanical deformation, sorption/desorption, and transport property of gas on the permeability variation of coal seams were researched.[10−21] These permeability models are broadly classified into two types of strain-based models that consider volumetric deformation of the coal and stress-based models that consider geomechanical deformation.[22,23] With the advancement of the recognition of physical properties of the reservoir, the conceptual model of naturally fractured reservoirs has been improved from a single-porosity single-permeability model[14,24] to a dual-porosity single-permeability (fracture permeability) model,[9,25] a dual-porosity dual-

Received: May 31, 2022
Accepted: August 16, 2022
Published: August 25, 2022

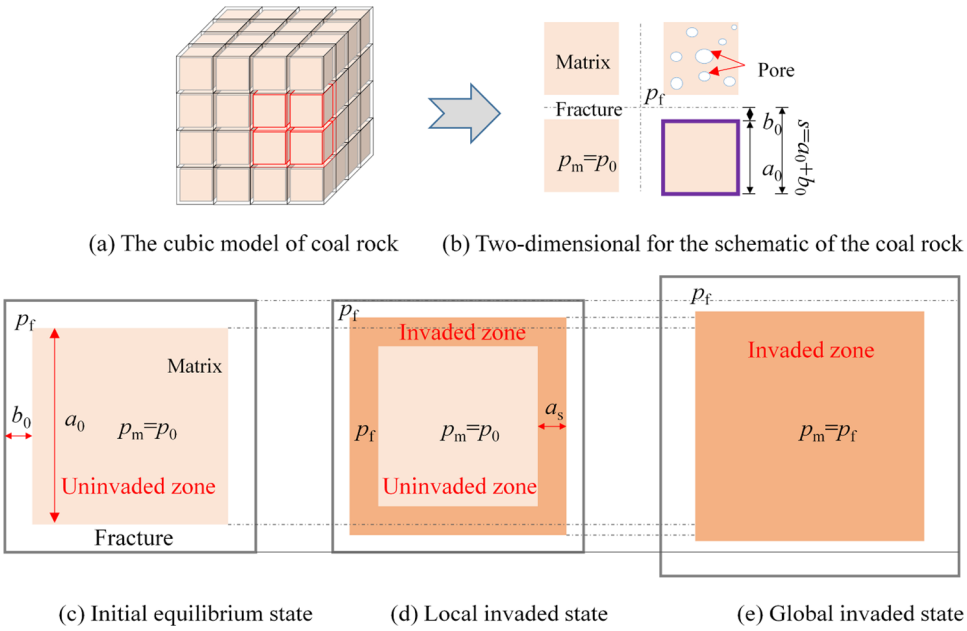

Figure 1. Conceptual model of coal rock (a, b) and the illustration of the initial equilibrium state to the global invaded state (c–e).

permeability model (both matrix and fracture permeability),[15,26] and a triple-porosity dual-permeability (both fracture permeability and inorganic permeability).[27] The factors affecting reservoir permeability also extend from a single mechanic effect[11,28] to adsorption-induced strain effects[10,24,29−31] or even coupled with the effect of slip flow.[32−37] Modeling the permeability evolution of coal during CBM recovery or CO_2-ECBM is an attractive interest area with numerous models being proposed. For instance, Zhou et al.[38] investigated the effect of CO_2−CH_4 interaction on porosity and permeability during CO_2-ECBM recovery and developed a related model coupling binary gas flow and coal deformation. Wu et al.[15] analyzed the anisotropic evolution of permeability due to gas adsorption and investigated the effects of in situ stresses and fracture aperture on pressure responses during gas production in COMSOL. Fang et al.[39] constructed a dynamic permeability prediction model by considering the law of matrix permeability and fracture permeability during CO_2-ECBM recovery. Fan et al.[9] established a model for the evolution of fracture permeability, considering the THMC coupling of different fields, concluding that neglecting water migration would overestimate gas production and neglecting heat transfer would underestimate gas production.

Admittedly, previous studies have been successful in predicting reservoir permeability to some extent, and there are still gaps in the knowledge of the evolution of reservoir permeability. As the difference in matrix and fracture permeability, the injected gas is only adsorbed near the fracture wall at the beginning, while the swelling strain of the remaining matrix will not change.[40−43] The gas diffusion (or invaded) process will continue for a considerable period of time due to the extremely low permeability of the matrix. Therefore, the temporal variability of the invaded region (see Figure 1c–e) will result in a transformation of the swelling strain from an initial local swelling located near the fracture surface that completely reduces the fracture aperture to an eventual global swelling strain that affects the bulk volume.[43,44] And this invaded process becomes more complicated owing to the presence of the gas mixture. However, earlier models tend to ignore the matrix permeability without considering the effect of time-dependent swelling on permeability and are even less able to consider this complex gas invasion for CO_2-ECBM recovery involving binary gas.

In this paper, coal is considered as a dual-porosity dual-permeability medium based on the true volume of REV; we accurately consider the elastic deformation caused by the effective stress change in the matrix and fracture, the swelling/shrinkage of the matrix caused by the adsorption/desorption effect, and the convection and diffusion of the binary gas in the matrix and fracture. Moreover, the contribution of matrix swelling strain to permeability is quantified by an invaded volume fraction that accounts for the gas intrusion process involving binary gases. In this way, a permeability evolution model coupling solid deformation and fluid flow for a binary gas two-phase flow in gas−water is established. Also, we implement this model onto COMSOL by introducing two new PDE modules to explore the evolution of permeability during the 10 000 day field experiment of CO_2-ECBM and then analyze the effects of gas injection pressure, initial water saturation, and initial permeability of the matrix and fracture to capture the key factors that affect CO_2-ECBM recovery.

2. CO_2-ECBM MODEL DEVELOPMENT

The flow becomes multiphase during CO_2-ECBM when groundwater is present in the coal seams. The porosity and permeability affect the flow of water and gas, and the pressure changes caused by the flow of water and gas, in turn, affect the evolution of porosity and permeability. Thus, the establishment of the dynamic permeability evolution model under the combined effects of stress, pressures of water and gas, and adsorption/desorption will be introduced in this section. The basic assumptions in establishing the model are as follows:[45]

(1) CBM reservoir is a poroelastic medium with dual porosity and dual permeability.

(2) The reservoir temperature is constant.

https://doi.org/10.1021/acsomega.2c03377
ACS Omega 2022, 7, 31167−31182

(3) CO_2 and CH_4 adsorptions in the CBM reservoir are competitive, both following Langmuir isotherms, and adsorption and desorption only occur in the matrix.
(4) The matrix system only contains the gas phase, and the fracture system contains both the gas and water phases. The two phases are immiscible, and there is no material transfer between the phases.
(5) CO_2 and CH_4 coexist in the fracture and the matrix, and the free gas conforms to the ideal gas law.
(6) Strain is infinitesimal.

2.1. Concept of Invaded Volume Fraction (IVF). The gas invaded from the fracture to matrix, during the gas injection process (shown in Figure 1c–e), is very slow, which is usually represented by the invaded volume friction defined as follows[43]

$$f_{inv} = \frac{a_0^3 - (a_0 - 2a_s)^3}{a_0^3}, (a_0 - 2a_s \geq 0) \tag{1}$$

where a_0 is the initial matrix width (m) and a_s is the dynamic invaded depth (m), which is dependent on the diffusivity of CO_2, D_2 (m^2/s), and time, t (s), and equals $\sqrt{D_2 t}$.[43] Especially, the value of f_{inv} ranges from 0 to 1 ($f_{inv} = 1$ when $a_s = a/2$; $f_{inv} = 0$ when $a_s = 0$). The sorption strain of the gas mixture, related to the properties of each gas component, can be described by an extended Langmuir isotherm equation[9,46]

$$\begin{cases} \varepsilon_{ms} = \dfrac{\sum \varepsilon_{Li} b_i p_{mi}}{1 + \sum b_i p_{mi}} \\ \varepsilon_{ms0} = \dfrac{\sum \varepsilon_{Li} b_i p_{mi0}}{1 + \sum b_i p_{mi0}} \end{cases} \tag{2}$$

where i is 1 or 2, and subscripts 1 and 2 represent CH_4 and CO_2, respectively; ε_{ms} represents the matrix swelling strain caused by adsorption/desorption. Subscript 0 represents the initial state, ε_L is the Langmuir-type strain coefficient, and $b_i = 1/p_{Li}$(1/Pa). When injecting CO_2 into the coalbed methane reservoir, we assumed that the matrix volume of the invaded segment contains the CO_2, and the uninvaded matrix volume contains the CH_4 only. The matrix strain increment induced by the gas invading process is

$$\Delta\varepsilon_{ms} = f_{inv}\left(\frac{\varepsilon_{L2} p_{m2}}{p_{m2} + p_{L2}} - \frac{\varepsilon_{L1} p_{m1}}{p_{m1} + p_{L1}}\right) \tag{3}$$

where p_m is the gas pressure of the matrix (Pa), and subscripts 1 and 2 represent the pressure induced by CH_4 and CO_2, respectively. Since the sorption strain of the matrix partly corresponds to the bulk strain and the remaining contributes to the reduction of the fracture,[17,47] we can address the matrix sorption strain increment as $f_{inv}\,\Delta\varepsilon_{ms}$ (corresponding to the bulk strain) and $(1 - f_{inv})\,\Delta\varepsilon_{ms}$ (corresponding to the fracture aperture)

$$\Delta\varepsilon_{ms} = f_{inv}\,\Delta\varepsilon_{ms} + (1 - f_{inv})\Delta\varepsilon_{ms} \tag{4}$$

And the increment of bulk volume and the reduction of fracture volume caused by matrix sorption can be expressed as

$$\Delta V_{bs} = f_{inv}\,\Delta V_{ms} \tag{5}$$

$$\Delta V_{fs} = -(1 - f_{inv})\Delta V_{ms} \tag{6}$$

The matrix volume increment induced by adsorption is

$$\Delta V_{ms} = V_{m0}\Delta\varepsilon_{ms} \tag{7}$$

where V_{m0} is the initial matrix volume (m^3).

Therefore, the relationship between the bulk swelling strain increment and matrix swelling strain increment can be known from the definition of the bulk swelling strain increment

$$\Delta\varepsilon_{bs} = \frac{\Delta V_{bs}}{\Delta V_{b0}} = \frac{f_{inv} V_{m0}\Delta\varepsilon_{ms}}{\Delta V_{b0}} \approx \frac{f_{inv}\Delta\varepsilon_{ms}(V_{m0} + V_{f0})}{\Delta V_{b0}} = f_{inv}\,\Delta\varepsilon_{ms} \tag{8}$$

where V_{b0} and V_{f0} are the initial volume of coal bulk and fracture (m^3), respectively.

2.2. Permeability Evolution Model Based on IVF. We consider CBM reservoirs as dual elastic media in Figure 1. The effective stress, following the effective stress principle,[48] can be expressed as

$$\begin{cases} \sigma_{em} = \sigma - (\alpha p_m + \gamma p_f) \\ \sigma_{ef} = \sigma - \gamma p_f \end{cases} \tag{9}$$

where subscripts m and f represent the matrix and fracture, respectively, p represents the gas pressure in the pores (Pa), σ represents the mean principal stress (Pa), $\alpha = 1 - K/K_m$, $\gamma = 1 - K_f/K_m$ are the Biot coefficients for the matrix and fracture, respectively, and K, K_m, and K_f are the bulk modulus of the dual-porosity media, the matrix and fracture system (Pa), respectively.

2.2.1. Fracture Permeability. The gas pressure of the unreacted binary mixed gas follows Dalton's law and can be expressed as[46]

$$\begin{cases} p_m = p_{m1} + p_{m2} \\ p_f = p_{f1} + p_{f2} \end{cases} \tag{10}$$

where subscripts 1 and 2 represent the gas pressure caused by CH_4 and CO_2, respectively. Under the condition of robustly considering the elastic deformation of the matrix and fracture and the adsorption/desorption effect, we can express the coal volume strain $\Delta\varepsilon_v$ as[27]

$$\Delta\varepsilon_v = -\frac{a^3}{s^3 K_m}\Delta\sigma_{em} - \frac{s^3 - a^3}{s^3 K_f}\Delta\sigma_{ef} + \Delta\varepsilon_{bs} \tag{11}$$

where s is the fracture spacing (m), $\Delta\sigma_{em}$ and $\Delta\sigma_{ef}$ are the change of the effective stress of matrix and fracture (Pa), respectively, and $\Delta\varepsilon_{bs}$ is the bulk swelling strain. Combining eqs 9–10 and rewriting eq 11, we can obtain

$$\Delta\sigma_{ef} = \Delta\sigma - \gamma\Delta p_f = \frac{1}{\frac{1}{K_f} - \frac{a^3}{s^3}\left(\frac{1}{K_f} - \frac{1}{K_m}\right)}\left(\frac{a^3}{s^3 K_m}\alpha\Delta p_m + \Delta\varepsilon_{bs} - \Delta\varepsilon_v\right) \tag{12}$$

As K_m is several magnitudes larger than K_f ($1/K_f - 1/K_m \approx 1/K_f$), eq 12 can be simplified to

$$\Delta\sigma_{ef} = \Delta\sigma - \gamma\Delta p_f = \frac{s^3 K_f}{s^3 - a^3}\left(\frac{a^3}{s^3 K_m}\alpha\Delta p_m + \Delta\varepsilon_{bs} - \Delta\varepsilon_v\right) \tag{13}$$

https://doi.org/10.1021/acsomega.2c03377
ACS Omega 2022, 7, 31167–31182

According to the relationship between the volumetric strain and linear strain in the theory of elasticity, we obtain the change in fracture aperture Δb (m) as

$$\Delta b = \frac{b}{3K_f}\Delta\sigma_{ef} \tag{14}$$

Then, the fracture porosity ϕ_f can be expressed as

$$\phi_f = \phi_{f0}\left(1 + \frac{\Delta b}{b}\right) \tag{15}$$

Solving eqs 13−15, the porosity model of the fracture is

$$\phi_f = \phi_{f0}\left(1 + \frac{s^3}{3(s^3-a^3)}\left(\frac{a^3}{s^3K_m}\alpha\Delta p_m + f_{inv}\Delta\varepsilon_{ms} - \Delta\varepsilon_v\right)\right) \tag{16}$$

Based on the cubic law, the fracture permeability evolution model is

$$\frac{k_f}{k_{f0}} = \left(\frac{\phi_f}{\phi_{f0}}\right)^3 = \left[\left(1 + \frac{s^3}{3(s^3-a^3)}\left(\frac{a^3}{s^3K_m}\alpha\Delta p_m + f_{inv}\Delta\varepsilon_{ms} - \Delta\varepsilon_v\right)\right)\right]^3 \tag{17}$$

where the terms in parentheses on the right express the contributions to the fracture permeability from fluid pressure, adsorption, and mechanical deformation, respectively.

2.2.2. Matrix Permeability. According to eqs 9 and 12, the effective stress change in the matrix can be expressed as

$$\Delta\sigma_{em} = \Delta\sigma_{ef} - \alpha\Delta p_m = \frac{s^3K_f}{s^3-a^3}\left(\frac{(K_f+K_m)a^3 - K_ms^3}{K_mK_fs^3}\alpha\Delta p_m + \Delta\varepsilon_{bs} - \Delta\varepsilon_v\right) \tag{18}$$

Assuming that the matrix volume is V_m (m^2) and the matrix pore volume is V_p (m^2), the matrix porosity may be written as

$$\phi_m = \frac{V_p}{V_m} \tag{19}$$

Differentiating eq 19 yields

$$d\phi_m = d\left(\frac{V_p}{V_m}\right) = \frac{V_p}{V_m}\left(\frac{dV_p}{V_p} - \frac{dV_m}{V_m}\right) \tag{20}$$

Therefore, integrating both sides of the equation and taking the natural exponent of the results leads to

$$\frac{\phi_m}{\phi_{m0}} = \exp(\Delta\varepsilon_p - \Delta\varepsilon_m) \tag{21}$$

The volumetric change of the matrix is determined by the combined effect of effective stress and adsorption/desorption. When the matrix volume varies, the matrix pore also changes accordingly. Taking the effective stress and adsorption/desorption into consideration, we can define the volumetric strain for the matrix as

$$\Delta\varepsilon_m = -\frac{\Delta\sigma_{em}}{K_m} + \Delta\varepsilon_{ms} \tag{22}$$

Considering that the modulus of coal strain K_s is several magnitudes larger than the modulus of the matrix K_m ($1/K_s + 1/K_m \approx 1/K_m$), the change of pore volume strain, associated with the matrix global strain and pore local strain,[26] can be rewritten as

$$\Delta\varepsilon_p = \Delta\varepsilon_V - \Delta\varepsilon_{ms} + \frac{p_m - p_f}{K_m} \tag{23}$$

Substituting eqs 18, 22, and 23 into eq 21, the porosity model of the matrix is

$$\frac{\phi_m}{\phi_{m0}} = \exp\left[\frac{(1-K_f)s^3 - a^3}{s^3-a^3}\Delta\varepsilon_v - \left(2 - \frac{K_fs^3}{s^3-a^3}f_{inv}\right)\Delta\varepsilon_{ms} - \frac{p_f - p_m}{K_m} + \frac{1}{s^3-a^3}\frac{(K_f+K_m)a^3 - K_ms^3}{K_m}\alpha\Delta p_m\right] \tag{24}$$

Again, taking the cubic law, the evolution of matrix permeability can be expressed as

$$\frac{k_m}{k_{m0}} = \exp\left[\frac{3(1-K_f)s^3 - 3a^3}{s^3-a^3}\Delta\varepsilon_v - 3\left(2 - \frac{K_fs^3}{s^3-a^3}f_{inv}\right)\Delta\varepsilon_{ms} - \frac{3(p_f - p_m)}{K_m} + \frac{3}{s^3-a^3}\frac{(K_f+K_m)a^3 - K_ms^3}{K_m}\alpha\Delta p_m\right] \tag{25}$$

From eq 25, we can acknowledge that the evolution of permeability is a function of mechanical deformation, induced from the change in stress and fluid pressure, and adsorption deformation, corresponding to the gas invaded.

2.3. Fluid Migration Model. In developing the fluid transport models for the balance equation of each component, we formulate the following assumptions: (1) the laminar flow of binary mixed gas in matrix pores or fracture obeys Darcy's law and (2) the diffusion of the binary gas mixture between the matrix and fracture follows Fick's law. For the matrix system, the basic variable is the gas pressure. For the fracture system, the basic variables are gas pressure and water saturation, whereas water pressure is a function of gas pressure and water saturation.

2.3.1. Matrix Flow Equation. The equilibrium equation in the matrix system contains convection and diffusion, and it also includes the conversion between free gas and adsorbed gas. The premise of the equation is that the gas flow is affected by both the pressure field (Darcy's law) and the concentration field (Fick's law); therefore, the velocities are added. The equation can be written as[1,49]

$$\frac{\partial m_{mi}}{\partial t} + \nabla(v_{mi}\cdot\rho_{mi}) + \nabla(-D_i\nabla m_{miF}) = -Q_{gmf} \tag{26}$$

where m_{mi} represents the gas content in the matrix including free gas and adsorbed gas (kg/m^3), and subscript i represents the gas of different components; ρ_{mi} is the gas density of component i with a relationship with the gas pressure as ρ_{mi} =

https://doi.org/10.1021/acsomega.2c03377
ACS Omega 2022, 7, 31167−31182

$\beta_i p_{mi}$ (kg/m^3), $\beta_i = M_i/RT$, M_i is the relative molecular mass (kg/mol), and T is the reservoir temperature (K). The second term represents the advective flux related to the gas phase. The third term represents the nonadvective flux corresponding to gas diffusion. The m_{mi} of each component can be expressed as[50]

$$m_{mi} = \rho_{mi}\phi_m + \rho_s\rho_{gai}\frac{V_{Li}b_i p_{mi}}{1 + \sum b_i p_{mi}} \tag{27}$$

where ρ_s is the reservoir density (kg/m^3), ρ_{gai} is the gas density under standard conditions (p_a = 0.103MPa), and v_{mi} is the advective velocity of gas migration in the matrix considering the Klinkenberg effect (m/s), which can be expressed as[51]

$$v_{mi} = -\frac{k_m}{\mu_m}\left(1 + \frac{b_k}{p_{mi}}\right)\nabla p_{mi} \tag{28}$$

where b_k is the Klinkenberg coefficient and μ_m is the viscosity of the mixed gas in the matrix pores, which can be expressed as[27]

$$\mu_m = \frac{\mu_1}{1 + \frac{p_{m2}}{p_{m1}}\sqrt{\frac{M_2}{M_1}}} + \frac{\mu_2}{1 + \frac{p_{m1}}{p_{m2}}\sqrt{\frac{M_1}{M_2}}} \tag{29}$$

where μ_i is the gas viscosity (Pa·s) and D_i is the dynamic diffusion coefficient (m^2/s), which can be defined as

$$D_i = \frac{\phi_m}{\phi_{m0}}D_{i0} \tag{30}$$

Q_{gmf} is the gas exchange between the matrix and fracture, which may be expressed as

$$Q_{gmf} = w\rho_{ga}(p_{mi} - p_{fi}) \tag{31}$$

where $w = 8\ (1 + 2/a^2)\ k_m/\mu_m$ is the transfer coefficient between the matrix and fracture.[15,50,52] Combining eqs 26−31, the expressions of gas migration of different components in the matrix are obtained.

For CH_4

$$\left[\phi_m + \frac{V_{L1}b_1\rho_s p_a(1 + b_2p_{m2})}{(1 + b_1p_{m1} + b_2p_{m2})^2}\right]\frac{\partial p_{m1}}{\partial t} - \left[\frac{V_{L1}b_1b_2\rho_s p_a p_{m1}}{(1 + b_1p_{m1} + b_2p_{m2})^2}\right]\frac{\partial p_{m2}}{\partial t} + p_{m1}\frac{\partial \phi_m}{\partial t} - \nabla\left[\left(\frac{k_m(p_{m1} + b_k)}{\mu_m} + D_1\phi_m\right)\nabla p_{m1}\right] = -wp_a(p_{m1} - p_{f1}) \tag{32}$$

For CO_2

$$\left[\phi_m + \frac{V_{L2}b_2\rho_s p_a(1 + b_1p_{m1})}{(1 + b_1p_{m1} + b_2p_{m2})^2}\right]\frac{\partial p_{m2}}{\partial t} - \left[\frac{V_{L2}b_1b_2\rho_s p_a p_{m2}}{(1 + b_1p_{m1} + b_2p_{m2})^2}\right]\frac{\partial p_{m1}}{\partial t} + p_{m2}\frac{\partial \phi_m}{\partial t} - \nabla\left[\left(\frac{k_m(p_{m2} + b_k)}{\mu_m} + D_2\phi_m\right)\nabla p_{m2}\right] = -wp_a(p_{m2} - p_{f2}) \tag{33}$$

2.3.2. Fracture Flow Equation. The coal fracture system contains binary gas and liquid water; hence, two mass conservation equations are needed.[1,53] The governing equations for gas and water can be defined as

$$\frac{\partial m_{fi}}{\partial t} + \nabla(v_{fgi}\cdot\rho_{fi}) + \nabla(-D_i\nabla m_{fiF}) = Q_{gmf} \tag{34}$$

$$\frac{\partial m_w}{\partial t} + \nabla(v_w\cdot\rho_w) = 0 \tag{35}$$

where subscript w indicates water, and m_{fi} and m_w represent the quality of gas and water in the fracture system (kg/m^3), respectively, which can be described as

$$m_{fi} = S_g\phi_f\rho_{fi} \tag{36}$$

$$m_w = S_w\phi_f\rho_w \tag{37}$$

where S_w and S_g represent the saturation of water and gas, respectively, and $S_g = 1 - S_w$.[54] ρ_w represents the density of water (kg/m^3). v_{fg} and v_w represent the gas velocity and water velocity of the fracture (m/s), respectively. Based on Darcy's law, which can be described as[9]

$$v_{fi} = -\frac{k_{fe}}{\mu_f}\nabla p_{fi} \tag{38}$$

$$v_w = -\frac{k_{we}}{\mu_w}\nabla p_w \tag{39}$$

where p_w represents water pressure (Pa), and k_{fe} and k_{we} represent the effective permeability of gas and water in the fracture system (m^2), respectively. Water pressure and the actual permeability of gas and water expressed in terms of effective permeability[55] can be described as

$$p_c = p_g - p_w \tag{40}$$

$$\begin{cases} k_{fe} = k_f k_{rg0} k_{rg} \\ k_{we} = k_f k_{rw0} k_{rw} \end{cases} \tag{41}$$

where p_c is the capillary pressure (Pa), p_g represents the gas pressure (Pa), k_{rg0} and k_{rw0} represent the end-point relative permeability of gas and water (m^2), respectively, and k_{rg} and k_{rw} represent the relative permeability of gas and water (m^2), respectively. The capillary pressure and relative permeability model proposed by ref 56 are expressed as

$$p_c = p_e(se)^{-1/\lambda} \tag{42}$$

https://doi.org/10.1021/acsomega.2c03377
ACS Omega 2022, 7, 31167−31182

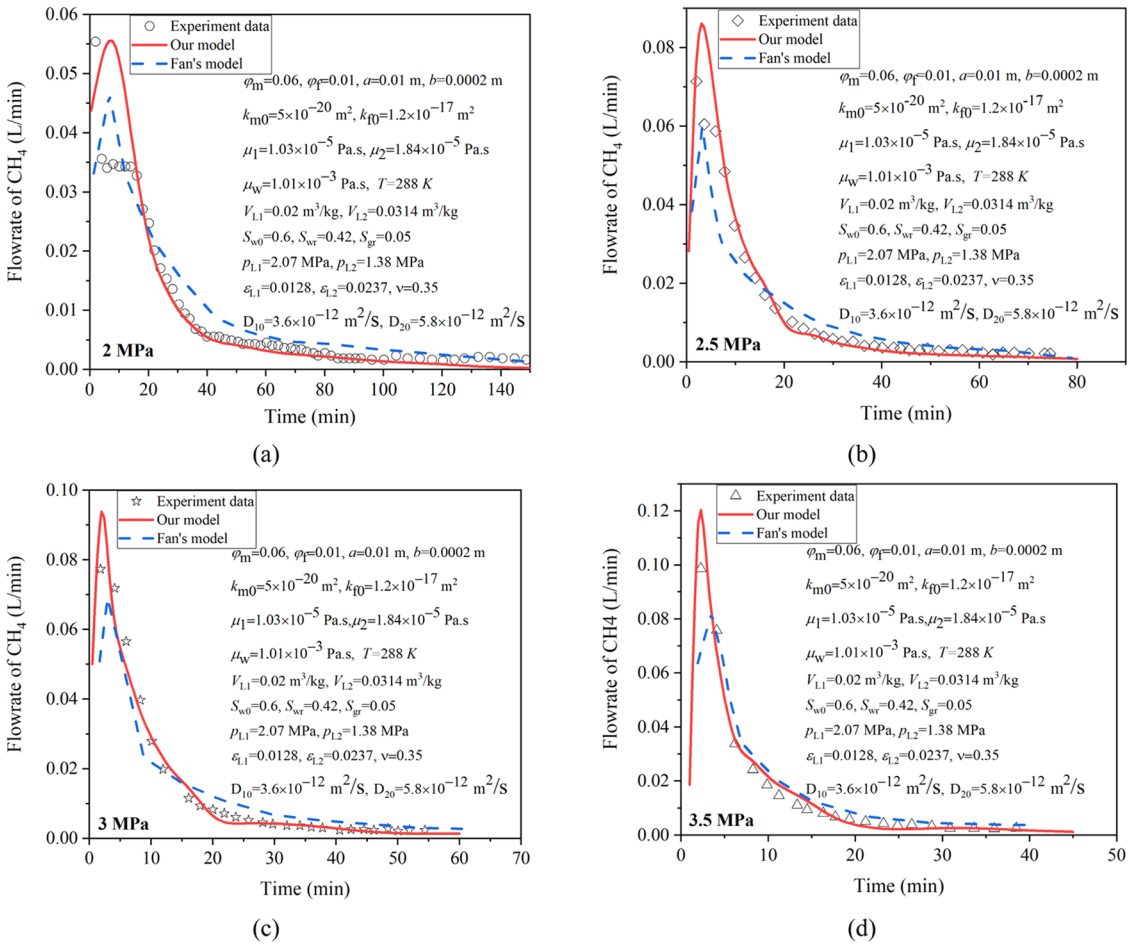

Figure 2. Comparison of our model with test data[5] and Fan's model[9] at various injection pressures: (a) 2 MPa, (b) 2.5 MPa, (c) 3 MPa, and (d) 3.5 MPa.

$$\begin{cases} k_{rg} = (1 - se)^2(1 - se^2) \\ k_{rw} = \sqrt{se}\,(1 - (1 - se^{1/m})^m)^2 \end{cases} \tag{43}$$

where p_e is the entry capillary pressure (Pa), λ is a function related to the pore size distribution, m is the relative permeability coefficient, and se is the effective saturation, expressed as

$$se = \frac{S_w - S_{wr}}{1 - S_{wr} - S_{gr}} \tag{44}$$

where S_{wr} is the irreducible water saturation, S_{gr} is the residual gas saturation, μ_w is the viscosity of water (Pa·s), and μ_f is the viscosity of mixed gas in the fracture system (Pa·s), which can then be written as

$$\mu_f = \frac{\mu_1}{1 + \frac{p_{f2}}{p_{f1}}\sqrt{\frac{M_2}{M_1}}} + \frac{\mu_2}{1 + \frac{p_{f1}}{p_{f2}}\sqrt{\frac{M_1}{M_2}}} \tag{45}$$

Combining eqs 34−45 yields the balance equation as the following.

For CH_4

$$[S_g\phi_f]\frac{\partial p_{f1}}{\partial t} + [-\phi_f p_{f1}]\frac{\partial S_w}{\partial t} + [S_g p_{f1}]\frac{\partial \phi_f}{\partial t} - \nabla\left[\left(\frac{k_{fe}p_{f1}}{\mu_f} + D_1 S_g \phi_f\right)\nabla p_{f1}\right] - \nabla[D_1\phi_f p_{f1}\nabla S_w] = -w\rho_{ga}(p_{m1} - p_{f1}) \tag{46}$$

For CO_2

$$[S_g\phi_f]\frac{\partial p_{f2}}{\partial t} + [-\phi_f p_{f2}]\frac{\partial S_w}{\partial t} + [S_g p_{f2}]\frac{\partial \phi_f}{\partial t} - \nabla\left[\left(\frac{k_{fe}p_{f2}}{\mu_f} + D_2 S_g \phi_f\right)\nabla p_{f2}\right] - \nabla[D_2\phi_f p_{f2}\nabla S_w] = w\rho_{ga}(p_{m2} - p_{f2}) \tag{47}$$

For water

$$[\phi_f\rho_w]\frac{\partial S_w}{\partial t} + [S_w\rho_w]\frac{\partial \phi_f}{\partial t} - \left[\left(\frac{k_{we}\rho_w}{\mu_w}\right)\nabla p_w\right] = 0 \tag{48}$$

2.4. Deformation Equation. Considering the influence of formation pressure change on reservoir deformation, the Navier equation of a dual-porosity medium can be expressed as[50]

https://doi.org/10.1021/acsomega.2c03377
ACS Omega 2022, 7, 31167−31182

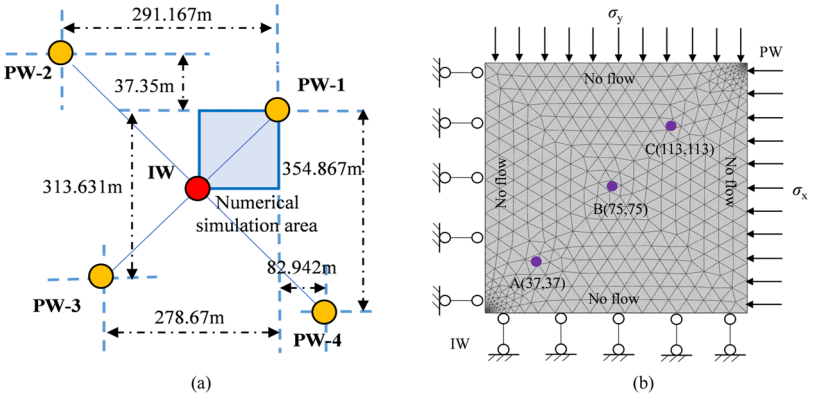

Figure 3. (a) Illustration of the five-point well for the CO_2-ECBM test and (b) model geometry for CO_2-ECBM simulation.

Table 1. Input Parameters Used in the Numerical Simulation

parameter	value	parameter	value
matrix width, a (m)	0.01	Langmuir constant of CH_4-induced strain, ε_{L1}	0.0128
fracture aperture, b(m)	0.0002	Langmuir constant of CO_2-induced strain, ε_{L2}	0.0237
initial permeability of the matrix, k_{m0} (m^2)	1×10^{-17}	Langmuir volume constant of CH_4, V_{L1} (m^3/kg)	0.0256
initial permeability of the fracture, k_{f0} (m^2)	1×10^{-14}	Langmuir volume constant of CO_2, V_{L2} (m^3/kg)	0.0477
porosity of the matrix, ϕ_{m0}	0.045	Langmuir pressure constant of CH_4, P_{L1} (MPa)	2.07
porosity of the fracture, ϕ_{f0}	0.011	Langmuir pressure constant of CO_2, P_{L2} (MPa)	1.38
density of coal, ρ_s (kg/m^3)	1.47×10^3	initial water saturation, S_{w0}	0.82
bulk modulus of the matrix, K_m (Pa)	1.2×10^{10}	irreducible water saturation, S_{wr}	0.42
bulk modulus of the fracture, K_f (Pa)	1.5×10^8	residual gas saturation, S_{gr}	0.05
Young's modulus of coal seam, E (GPa)	4	dynamic viscosity of CH_4, μ_1 (Pa·s)	1.34×10^{-5}
temperature, T (K)	338.8	dynamic viscosity of CO_2, μ_2 (Pa·s)	1.84×10^{-5}
coefficient, η	1	dynamic viscosity of water, μ_w (Pa·s)	1.01×10^{-3}
Klinkenberg factor, b_k (MPa)	0.76	diffusion coefficient of CH_4, D_{10} (m^2/s)	3.6×10^{-12}
entry capillary pressure, p_e (MPa)	0.1	diffusion coefficient of CO_2, D_{20} (m^2/s)	5.8×10^{-12}
capillary pressure model: coefficient, λ	2	relative permeability model coefficient, m	0.6
Poisson's ratio, ν	0.35	In situ stress of reservoir, σ (MPa)	6

$$Gu_{i,kk} + \frac{G}{1-2\nu}u_{k,ki} + f_i = \alpha p_{m,i} + \gamma p_{f,i} + K\varepsilon_{s,i} \quad (49)$$

where G is the shear modulus (Pa), u is the displacement (m), ν is Poisson's ratio, and f is the body force (N). The gas flow equations of CH_4 and CO_2 (eqs 32−33), mass conservation equations of CH_4, CO_2, and water (eqs 46−48), and deformation equation of formation (eq 49) together make up the multifield coupling model for dual-porosity media.

3. MODEL VALIDATION

To verify the suitability and feasibility of this model, we compare our model with the experimental data[5] and Fan's model[9] that of CO_2-ECBM under various injection pressures. The experiment was conducted at Chongqing University using coal samples recovered from the C1 coal seam in the Baijiao Coal Mine, Nanchuan Basin, China. Cylindrical coal samples had a diameter of 48.3 mm and a height of 98.2 mm. During the experiment, the temperature was set to 15 °C and the confining stress and axial stress were 6 MPa and 8 MPa, respectively. At the beginning of the experiment, CH_4 was injected under a constant gas injection pressure of 1.5 MPa to ensure gas pressure equilibrium in the sample. Then, under the constant confining stress and axial stress, CO_2 injection pressures of 2, 2.5, 3, and 3.5 MPa were applied at the top of the samples, and the pressures of CO_2 and CH_4 at the bottom outlet were kept at the atmospheric pressure. The initial CH_4 pressure of the coal sample is 1.5 MPa. All of the relevant parameters are listed in Figure 2a−d; most of them are obtained from the original research[5] and the related papers,[9,15,27] while the rest are obtained by fitting experimental data. Results in Figure 2 indicate that our model is in good agreement with the experimental data at different injection pressures, and the fit is better under the conditions of higher gas injection pressure than the lower. The seepage problem in the matrix−fracture of coal in our model is a bimodal pore system model, and the adsorption deformation is considered time-dependent. Thus, the flow rate of CH4 within the coal is more sensitive to the deformation than Fan's model.

4. CO_2-ECBM NUMERICAL SIMULATION

4.1. Model Description. To investigate the permeability evolution during a gas−water two-phase flow in the CO_2-ECBM mining of coal reservoirs, we build a 150 m × 150 m × 5 m model (see Figure 3b), which belongs to the upper right quadrant of a traditional five-point well configuration,[57] as shown in Figure 3a. The well diameter is 0.1 m for injection well (IW) and production well (PW). For the geomechanics boundary conditions, the left and bottom are zero-displacement-constrained, and in situ stress is applied on the top and right boundaries. For the gas flow boundary conditions, the bottom-hole pressures for PW and IW are 0.1 and 8 MPa, respectively, and the other boundaries are defined as no flow. As for the water flow boundary conditions, the pressures for

https://doi.org/10.1021/acsomega.2c03377
ACS Omega 2022, 7, 31167−31182

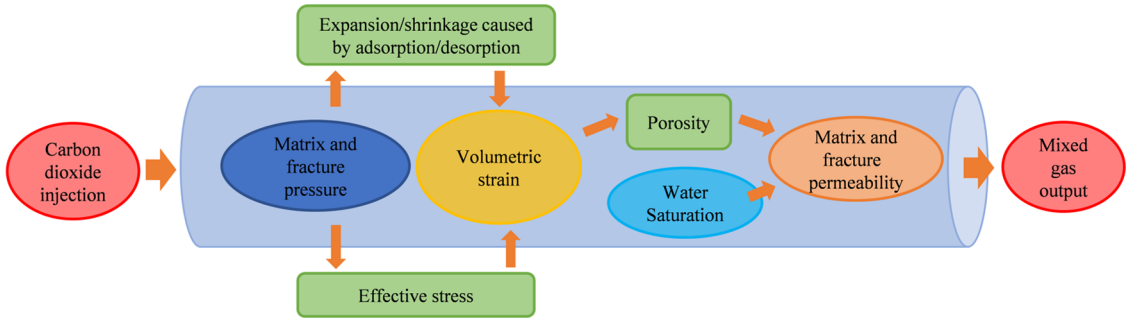

Figure 4. Key factors affecting permeability evolution in the matrix and fracture for CO_2-ECBM simulation.

PW and IW are the same as the gas flow boundary conditions; however, the IW and Pw are set as the Dirichlet boundaries with the prescribed values of Sw are 0 and 0.82, respectively.

The initial pressure of methane in the reservoir is 5.24 MPa, the initial pressure of carbon dioxide is set to be 0.1 MPa, the temperature is 338.8 K, the initial water saturation is 0.82, and the initial permeability is $k_m = 1 \times 10^{-17}$ m^2, $k_f = 1 \times 10^{-14}$ m^2. Other parameters required for simulation are listed in Table 1, as obtained from the literature.[5,9,15,27,39,58] The in situ stress of the reservoir is $\sigma_y = \sigma_x = 6$ MPa, and the simulations are run for 10 000 days. There are three reference points A (37, 37), B (75, 75), and C (113, 113) for simulation; we will analyze them in detail in the following section.

4.2. Simulation Results. We analyze the changes in gas pressure, permeability, and reservoir deformation of the matrix and fracture at different locations under the two-phase flow environment. The schematic in Figure 4 shows the key factors that could affect gas production behavior. As we all know, the injection of CO_2 and the production of CH_4 change the gas pressure, causing effective stress changes and adsorption/desorption to occur, which affects the evolutions of porosity and permeability of the reservoir. At the same time, the drainage alters the effective pore size for the gas flow in the fracture. Changes in the gas flow rate will also affect the changes in gas pressure, which, in turn, affects permeability. In the following, we will analyze the evolution of permeability and its mechanisms in detail by examining the pressure, strain, and methane and carbon dioxide contents of the reservoir.

Figure 5 shows the relationship between gas volume invaded friction (f_{inv}) and time during the process of CO_2-ECBM. It is worth mentioning that this time is not the duration of mining, but the time during which CO_2 arrives in a certain area and fully invades it. The f_{inv} increases with time, and the value ranges from 0 to 1. This means the matrix swelling strain from initially reducing the fracture aperture ($f_{inv} = 0$) to eventually affecting the bulk volume strain ($f_{inv} = 1$). The process of CO_2 invading the matrix takes about 100 days.

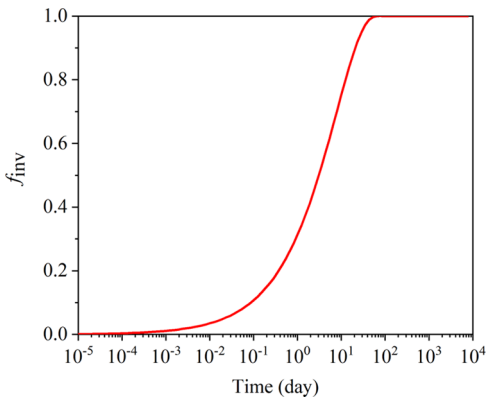

Figure 5. Evolution of the gas invaded volume fraction versus time.

4.2.1. Gas Pressure. Figure 6 shows the evolution of gas pressures in the matrix and fracture at A−C locations during the simulation period. Within the first 10 days, we clearly observe that the matrix gas pressure change occurs later than the fracture at the beginning. This phenomenon occurs because the gas exchange between the matrix and the outside world occurs through the fracture system. In addition, the pressure changes in the matrix and fracture show a common phenomenon; that is, in the beginning, the pressure at point A increases as CO_2 is injected; the pressure at point C decreases with the production of methane. At about 100 days, the increase of CO_2 at point B will cause the pressure to increase; however, the pressure increase at point C is more likely caused by the gas desorption from coalbed since the CO_2 has not traveled to this part. As the process continues, the pressure will reach a peak value and begin to decrease due to the long-term production of CH_4.

4.2.2. Permeability. The permeability evolution contours in the simulated area are shown in Figure 7. We find that the change in permeability is most pronounced during the first 3000 days of the CO_2 injection process. The permeability of the matrix and fracture evolves in a similar manner. That is, the reduction in distance from the IW enhances the permeability. In contrast, the permeability decreases with distance from the PW. The permeability change of the fracture is more profound with greater reduction compared with the matrix permeability. To understand how permeability evolves more intuitively, we plot the change of permeability over time at reference points, as shown in Figure 8.

After the permeability at point A reaches the peak point M, it enters stage II and the net permeability starts to decrease, as illustrated in Figure 8. Due to the extra low porosity of the reservoir, the injected gas diffusing from IW to PW will take a long time. Therefore, the time of permeability evolution to stage II increases with the distance from IW, that is, point B is about 100 days, and point C is about 500 days. Permeability in stage I is mainly controlled by effective stress, while in stage II, it is primarily affected by gas adsorption/desorption. Importantly, both adsorption and desorption exist in the process of CO_2 replacing CH_4. Since the Langmuir volume constant of CO_2 is larger than CH_4, as a result, the expansion caused by CO_2 adsorption is larger than the contraction caused by the desorption of CH_4. Furthermore, the influencing factors on permeability evolution at point C are more complicated.

https://doi.org/10.1021/acsomega.2c03377
ACS Omega 2022, 7, 31167−31182

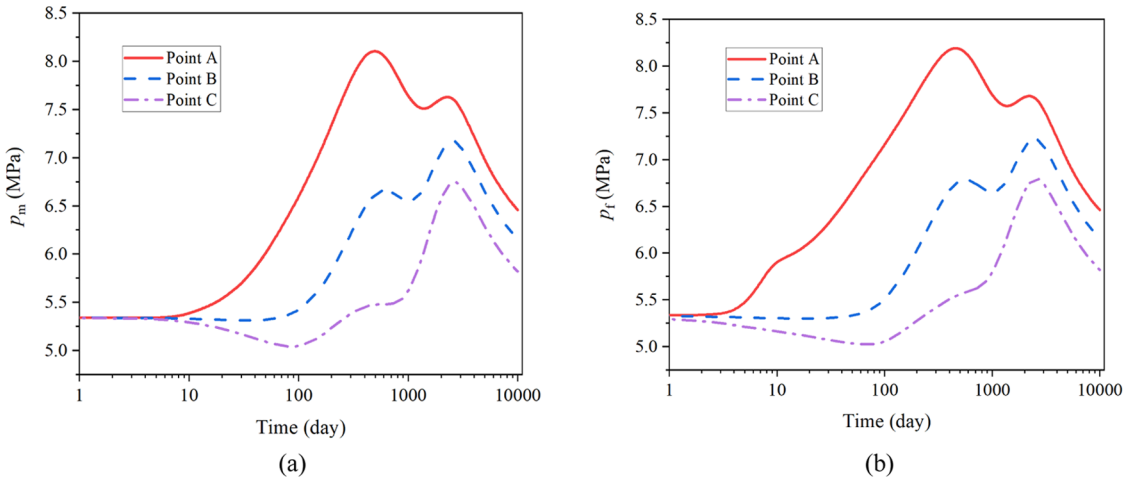

Figure 6. Evolution of gas pressure in the matrix and fracture system during CO_2-ECBM: (a) gas pressure in the matrix and (b) gas pressure in the fracture.

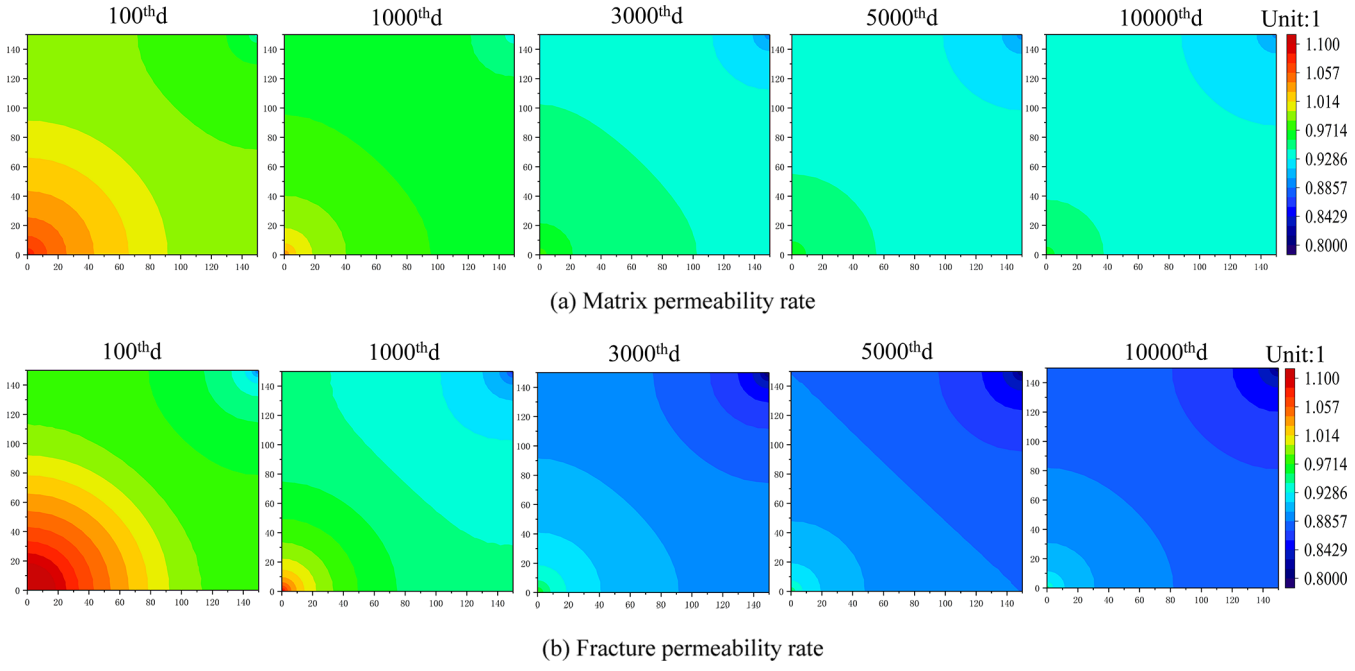

Figure 7. Evolution of coal matrix and fracture permeability rate in the model during CO_2-ECBM.

With reference to Figure 6, the increase in the matrix and fracture pressure causes the effective stress to decrease, resulting in an increase in porosity and permeability. Concurrently, the increased pressure leads to CO_2 adsorption and CH_4 desorption and associated swelling/shrinkage strains. When the CO_2 content is sufficient, the adsorption strain is greater than the desorption strain (Figure 9 shows increased adsorption strain); hence, the process is considered to be matrix expansion. The expansion of the matrix narrows the fracture aperture, which also compresses the matrix pores, so that the permeability of the matrix and the fracture tend to decrease. The result of the competition between these two processes causes the net permeability to decline.

4.2.3. Gas Content. The evolution of CH_4 and CO_2 gas contents (kg/m^3) in the simulated area is shown in Figure 10. The CH_4 content is always centered around the PW, and it gradually increases toward the IW. Conversely, the CO_2 content is always centered around the IW and gradually decreases toward the PW. Following, we draw a straight line from the IW to the PW and plot a function between the gas content and distance away from the IW at different times, as shown in Figure 11. It can be seen that, at all times, the farther away from the IW, the lower the gas content. Gas contents in the vicinity of PW drop sharply. As CO_2 injection continues, the methane gas content in the simulated area keeps decreasing, and the carbon dioxide content keeps increasing. A larger degree of change is seen in the first 3000 days. Figure 12 shows the CH_4 production rate, CO_2 injection rate, and water production rate during the 5000 days of injection. During the first 1000 days, the water production rate declines exponentially. Therefore, the reduction of water saturation in the fracture system increases the effective gas permeability and the flow rate, so the gas production rate continues to increase. At about 1000 days, the water production rate basically reaches the minimum value, while the gas production rate reaches the maximum value. For the storage of CO_2, the injection rate

https://doi.org/10.1021/acsomega.2c03377
ACS Omega 2022, 7, 31167−31182

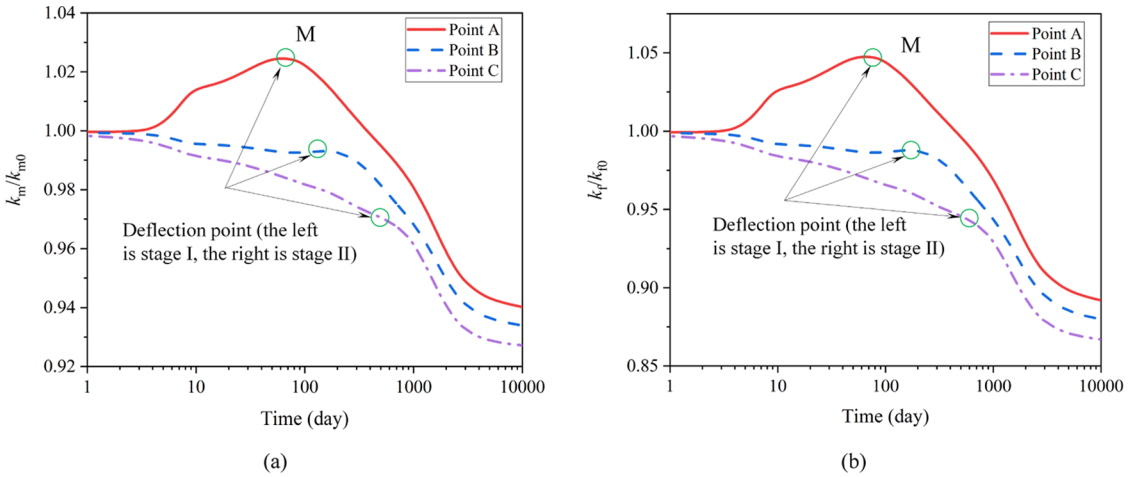

Figure 8. Evolution of the permeability ratio at three reference points (A, B, C) during CO_2-ECBM: (a) matrix permeability ratio and (b) fracture permeability ratio.

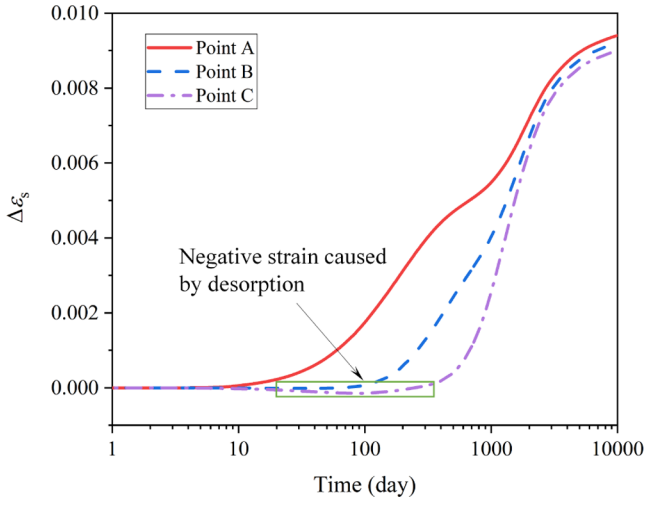

Figure 9. Adsorption-induced strain at three reference points (A, B, C) during CO_2-ECBM.

reaches the maximum within a short time and is then followed by a downward trend. This is because the CO_2 pressure increases rapidly near the IW in a short time. However, due to the low effective gas permeability, CO_2 cannot reach deep into the reservoir within a short time, resulting in the accumulation of CO_2 around the IW, which limits the pressure differential between the inside and outside of the IW and thus reduces the carbon dioxide storage rate. As drainage progresses, the gas migration path in the fracture increases and the gas velocity increases. Therefore, as CO_2 around the IW migrates further into the reservoir, we observe an increased CO_2 injection rate until it reaches the second, but relatively small, peak.

5. RESULTS AND DISCUSSION

We will discuss how the key factors impact reservoir performance in this section. These factors include carbon dioxide injection pressure, initial water saturation, and initial permeability of the matrix and fracture system.

5.1. Injection Pressure. Taking A and C as reference points, it is known from the discussions above that permeability evolution depends on two competing processes: effective stress and adsorption/desorption. Changing CO_2 injection pressure can affect the changes of the two processes simultaneously. Therefore, we perform research on the evolution of permeability at different locations when the CO_2 injection pressure is 4, 6, and 8 MPa.

The effects of different injection pressures on permeability and adsorption are demonstrated in Figures 13 and 14, respectively. Figure 13 indicates that under the same gas injection pressure, the permeability evolution of the matrix and fracture is similar: the higher the gas injection pressure, the more dynamic the permeability evolution. For the same position, we find that stage I of permeability evolution will end up earlier at higher injection pressure. Moreover, the permeability at about 10 000 days will decrease with the increasing injection pressure. And the difference in permeability values at different locations will become smaller with the higher injection pressure. In the case of higher injection pressure, the permeability peak appears earlier and stage II starts earlier due to the lower effective stress at point A. In addition, we find that the evolution of permeability at point C is almost opposite to that at point A when using different gas injection pressures. In Figure 13, the permeability at point C of stage I increases with the decreasing injection pressure, and from the beginning of stage II (point E) to equilibrium state, the permeability ends up higher at the lowest injection pressure. The mechanism of this phenomenon is that higher injection pressure will increase the pressure in coal seam; thus, the adsorption swelling of CO_2 will exceed the desorption of CH_4, leading to a lower permeability. Figure 14 shows that the desorption at point C is negatively correlated with the gas injection pressure. In other words, when the gas injection pressure decreases, the maximum strain caused by desorption increases. Therefore, it can be inferred that from the beginning of stage II to point E, the desorption has a dominant influence on permeability.

5.2. Initial Water Saturation. In this work, the initial water saturations of 0.64, 0.74, and 0.84 are considered to explore the effects of different initial water saturations on the evolution of permeability. Figure 15 illustrates that the smaller the initial water saturation, the higher the peak matrix and fracture permeability at point A and the lower the permeability at point C in the first 100 days. Combining with the adsorption strain at points A and C in Figure 16, obviously, the lower initial water saturation of reservoir, the earlier adsorption occurs, and the higher water saturation will limit gas

https://doi.org/10.1021/acsomega.2c03377
ACS Omega 2022, 7, 31167−31182

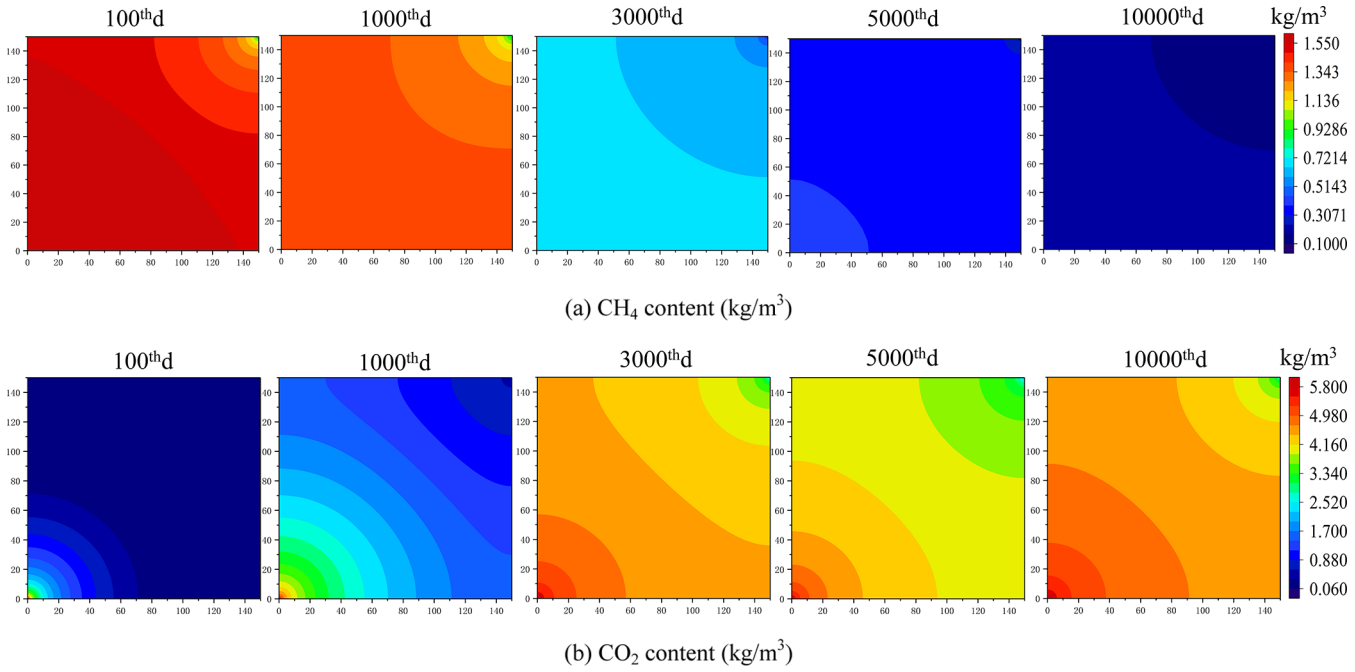

Figure 10. Distribution of CH_4 and CO_2 contents in the model during CO_2-ECBM.

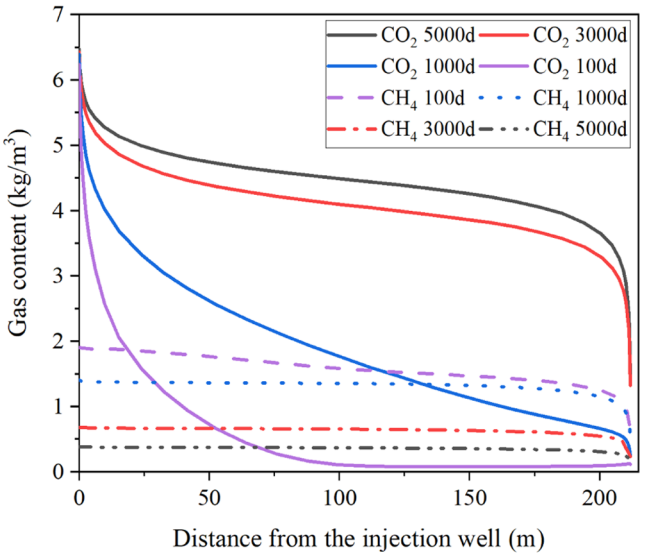

Figure 11. Variation of CH_4 and CO_2 contents in the reservoir with the distance away from the gas injection well.

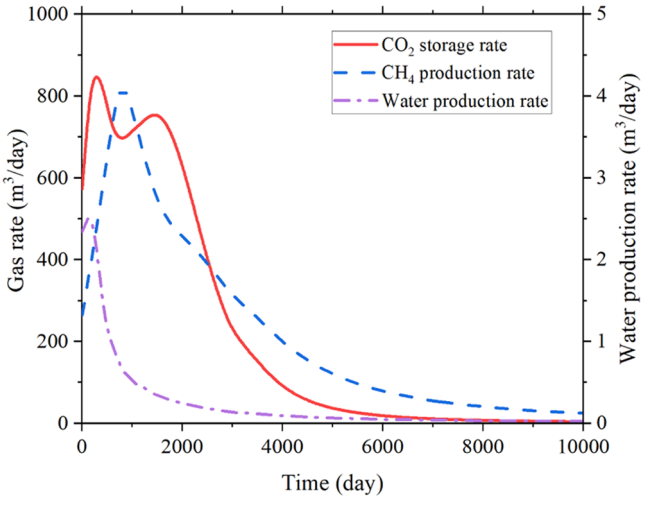

Figure 12. Water and gas production rates and CO_2 injection rate during CO_2-ECBM.

adsorption to enhance the permeability. However, as the injection continues long enough, the permeability tends to be independent of water saturation and equal to the equilibrium state. Similarly, after a sufficient period of time, the adsorption strains show no dramatic difference. Figure 17 displays the effect of the initial water saturation of the reservoir on gas migration. We find that faster migration is associated with lower initial water saturation until a certain time. A higher water saturation will occupy more flow channels and reduce the percentage of gas content before the system equilibrates.

5.3. Initial Permeability. Reasonable values of the initial permeability of the matrix and fracture in three cases are selected within the range of available literature to examine the effect of initial reservoir permeability on the gas migration performance, and the input parameters for these cases are summarized in Table 2. The evolution of the matrix and fracture permeability at different initial permeability values is shown in Figure 18. We can see that the initial permeability has a significant impact on gas migration. As the initial permeability decreases, stage II occurs late and the final decrease in permeability becomes smaller. The reason for this is that the smaller the initial permeability, the later the adsorption occurs near the production well, as shown in Figure 19. Consequently, a smaller adsorption strain causes a smaller decrease in permeability. The difference in initial permeability, however, has little effect on the degree of change in the matrix and fracture permeability at different locations, as shown in Figure 18, where three cases are plotted with the same $\Delta k_{mL}/\Delta k_{fL}$.

In Figure 20, the ratio between methane and carbon dioxide concentration is plotted. It is found that the increase in initial permeability has accelerated the gas migration rate in the

https://doi.org/10.1021/acsomega.2c03377
ACS Omega 2022, 7, 31167−31182

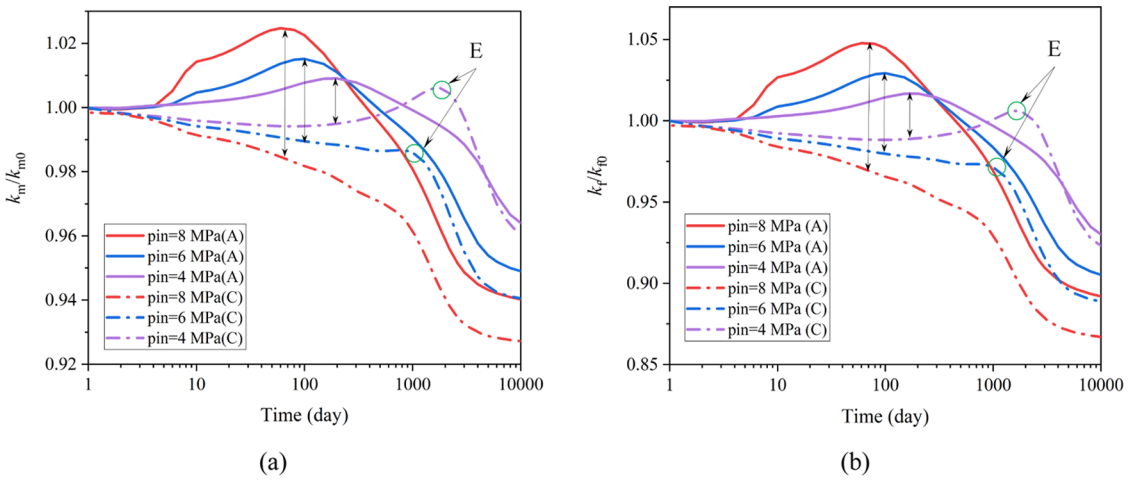

Figure 13. Permeability evolution at reference points A and C with different gas injection pressures (E is the deflection point of adsorption/desorption) during CO_2-ECBM: (a) matrix permeability ratio and (b) fracture permeability ratio.

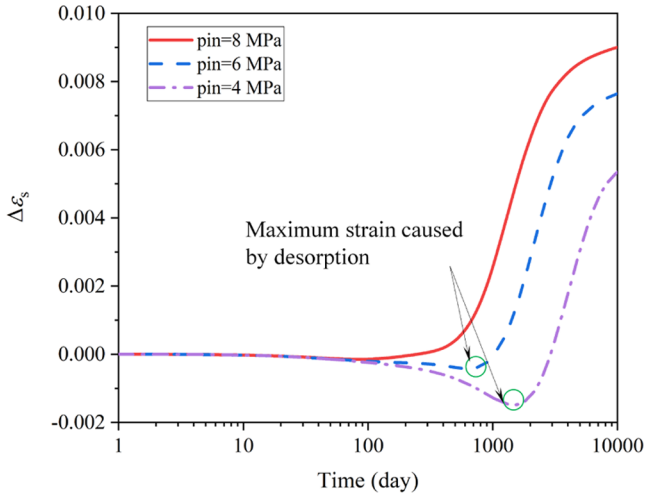

Figure 14. Adsorption strain at reference point C under different injection pressures during CO_2-ECBM.

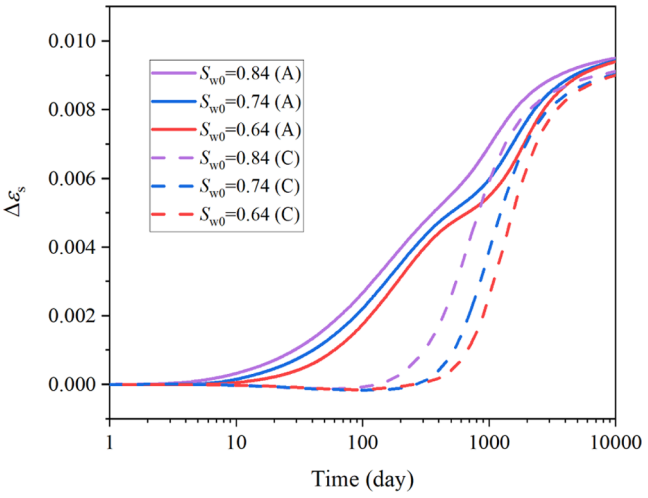

Figure 16. Adsorption-induced strain at reference points A and C under different initial water saturations during CO2-ECBM.

reservoir, and methane production and carbon dioxide storage have also increased during the same period. Clearly, it is important to take measures to increase the reservoir permeability before gas production in the field.

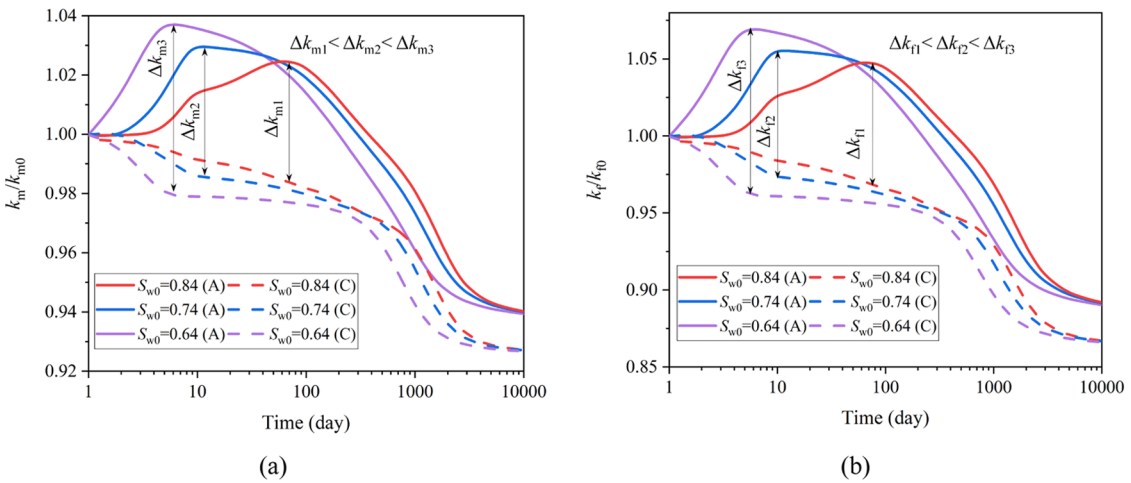

Figure 15. Permeability evolution at reference points A and C with different initial water saturations during CO_2-ECBM: (a) matrix permeability ratio and (b) fracture permeability ratio.

https://doi.org/10.1021/acsomega.2c03377
ACS Omega 2022, 7, 31167−31182

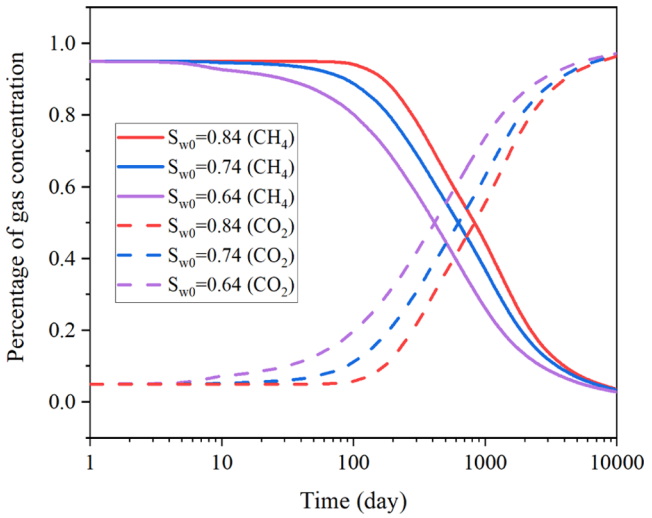

Figure 17. Variation of CH_4 and CO_2 content percentages at reference points A and C with different initial water saturations.

Table 2. Initial Permeability of Matrix and Fracture in Three Cases Used for Sensitivity Analysis

case	matrix (m^2)	fracture (m^2)
Case 1	10^{-17}	10^{-14}
Case 2	5×10^{-18}	5×10^{-15}
Case 3	1×10^{-18}	1×10^{-15}

6. CONCLUSIONS

We developed a multifield-coupled two-phase permeability evolution model by accurately taking into account the elastic deformation caused by the effective stress change in different media (matrix and fracture), the swelling/shrinkage deformation of the matrix caused by the adsorption/desorption effect, and both convective and diffusive flows in the matrix and fracture. Then, we verified the fidelity of our model by comparing against experimental data and applying it to a CO_2-ECBM field case. A comprehensive analysis of permeability evolution during 10 000 days of CO_2-ECBM was performed. Furthermore, we conducted a sensitivity analysis on three initial parameters including initial water saturation, initial

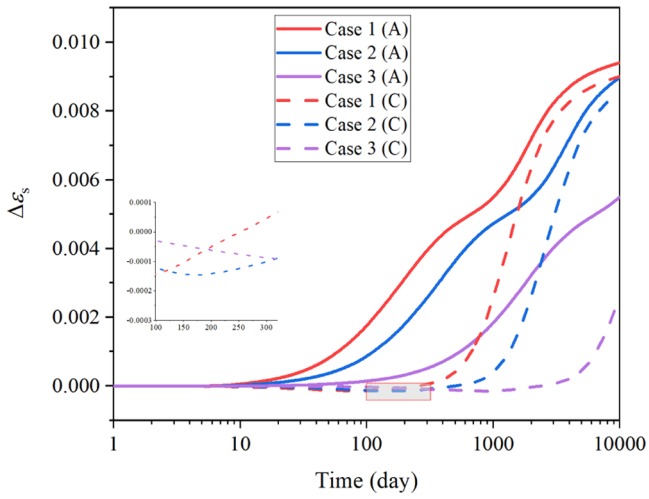

Figure 19. Adsorption-induced strain at reference points A and C under three different initial permeabilities during CO_2-ECBM.

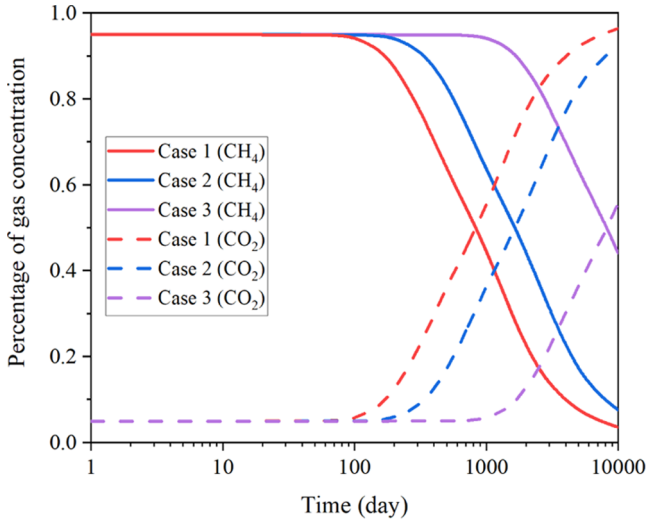

Figure 20. Variation of CH_4 and CO_2 content percentages at reference points A and C under three different initial permeabilities.

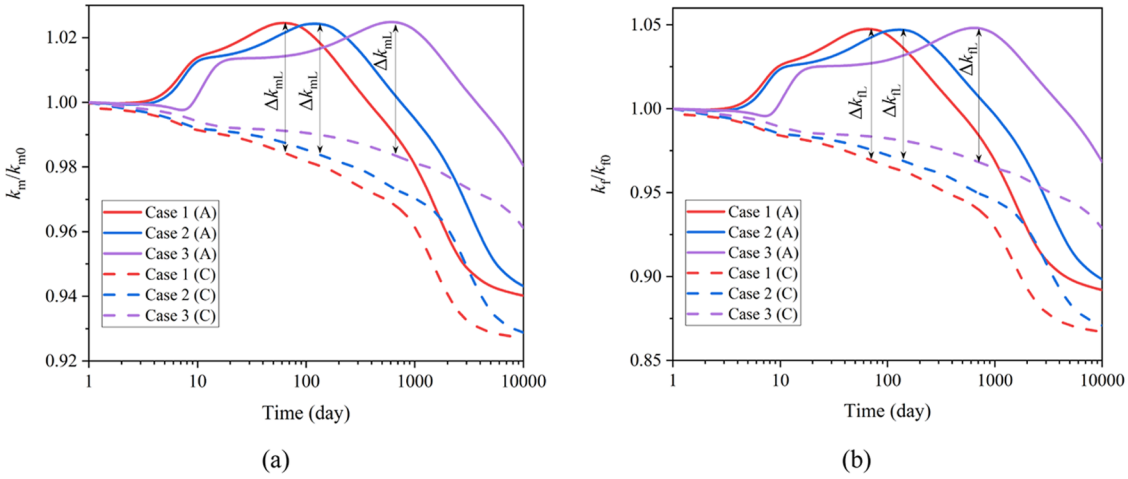

Figure 18. Permeability evolution at reference points A and C under three different initial permeabilities during CO_2-ECBM: (a) matrix permeability ratio and (b) fracture permeability ratio.

https://doi.org/10.1021/acsomega.2c03377
ACS Omega 2022, 7, 31167−31182

permeability, and gas injection pressure. The following conclusions can be drawn from this study:

(1) Significant difference exists in permeability evolution between the area near the IW and PW in the reservoir. This is the result of the combined effect of effective stress and adsorption/desorption. Therefore, it is very important to fully consider the permeability evolution at different locations in the entire area during CO_2-ECBM recovery. The permeability evolution process at any location can be approximately divided into two stages, and each stage is affected by the effective stress and adsorption/desorption to different degrees. In stage I, permeability is mainly dominated by effective stress, and in stage II, it is mainly dominated by adsorption/desorption.

(2) The higher the gas injection pressure, the greater the difference in permeability at different locations in the reservoir, and the lower the permeability at the same location. In addition, high injection pressure creates a faster gas migration velocity and a lower effective stress, which causes stage II of permeability evolution to appear earlier.

(3) The water in the reservoir has a negative effect on gas migration. Larger initial water saturation of the reservoir slows down the gas migration rate, resulting in delayed adsorption. Decreasing the initial water saturation causes the permeability of the matrix and fracture to change drastically and also causes stage II of permeability evolution to appear earlier. However, the difference in initial water saturation has a negligible effect on the reservoir performance when the injection time is long enough.

(4) The initial coal permeability has a great influence on the gas migration in the reservoir. Decreasing the initial permeability leads to a slower gas migration rate and delays the time for adsorption to take effect, which decreases the adsorption-induced strain. In addition, it also delays the start of stage II of permeability evolution and reduces the magnitude of decrease in permeability within the same amount of time.

AUTHOR INFORMATION

Corresponding Author

Zhiyong Xiao − *Shandong Provincial Key Laboratory of Civil Engineering Disaster Prevention and Mitigation, Shandong University of Science and Technology, Qingdao 266590, China; College of Civil Engineering and Architecture, Shandong University of Science and Technology, Qingdao 266590, China;* orcid.org/0000-0001-6055-0889; Email: xzyfly3_sdut@163.com

Authors

Gang Wang − *Shandong Provincial Key Laboratory of Civil Engineering Disaster Prevention and Mitigation, Shandong University of Science and Technology, Qingdao 266590, China; College of Civil Engineering, Fujian University of Technology, Fuzhou 350118, China; College of Civil Engineering and Architecture and State Key Laboratory of Mining Disaster Prevention and Control Co-founded by Shandong Province and the Ministry of Science and Technology, Shandong University of Science and Technology, Qingdao 266590, China*

Feng Xu − *Shandong Provincial Key Laboratory of Civil Engineering Disaster Prevention and Mitigation, Shandong University of Science and Technology, Qingdao 266590, China; College of Civil Engineering and Architecture, Shandong University of Science and Technology, Qingdao 266590, China; Urban Traffic Engineering Co., Ltd., CCCC First Navigation Engineering Bureau, Tianjin 300450, China*

Lu Zhang − *Shenzhen Water Planning and Design Institute Co., Shenzhen 518000, China*

Yujing Jiang − *State Key Laboratory of Mining Disaster Prevention and Control Co-founded by Shandong Province and the Ministry of Science and Technology, Shandong University of Science and Technology, Qingdao 266590, China*

Feng Jiang − *Shandong Provincial Key Laboratory of Civil Engineering Disaster Prevention and Mitigation, Shandong University of Science and Technology, Qingdao 266590, China; College of Civil Engineering and Architecture, Shandong University of Science and Technology, Qingdao 266590, China*

Chengcheng Zheng − *Shandong Provincial Key Laboratory of Civil Engineering Disaster Prevention and Mitigation, Shandong University of Science and Technology, Qingdao 266590, China; College of Civil Engineering and Architecture, Shandong University of Science and Technology, Qingdao 266590, China*

Complete contact information is available at: https://pubs.acs.org/10.1021/acsomega.2c03377

Notes

The authors declare no competing financial interest.

ACKNOWLEDGMENTS

This work was supported by the "Natural Science Foundation of China" (52079077). The source of support was gratefully acknowledged.

REFERENCES

(1) Kumar, H.; Elsworth, D.; Mathews, J. P.; Liu, J.; Pone, D. Effect of CO_2 injection on heterogeneously permeable coalbed reservoirs. *Fuel* **2014**, *135*, 509−521.

(2) Rundgren, E. J. Coal-Bed Methane Provides Less-Invasive Production Method. *Nat. Gas. Electr.* **2016**, *33*, 22−25.

(3) Godec, M.; Koperna, G.; Gale, J. CO_2-ECBM: a review of its status and global potential. *Energy Procedia.* **2014**, *63*, 5858−5869.

(4) Zheng, S.; Yao, Y.; Elsworth, D.; Liu, D.; Cai, Y. Dynamic Fluid Interactions during CO_2-Enhanced Coalbed Methane and CO_2 Sequestration in Coal Seams. Part 1: CO_2−CH_4 Interactions. *Energy Fuels* **2020**, *34*, 8274−8282.

(5) Yin, G.; Deng, B.; Li, M.; Zhang, D.; Wang, W.; Li, W.; Shang, D. Impact of injection pressure on CO_2−enhanced coalbed methane recovery considering mass transfer between coal fracture and matrix. *Fuel* **2017**, *196*, 288−297.

(6) Deng, B.; Yin, G.; Zhang, D.; Li, M.; Liu, Y.; Lu, J. Experimental investigation of fracture propagation induced by carbon dioxide and water in coal seam reservoirs. *Powder. Technol.* **2018**, *338*, 847−856.

(7) Mazzotti, M.; Pini, R.; Storti, G. Enhanced coalbed methane recovery. *J. Supercrit. Fluids* **2009**, *47*, 619−627.

(8) Wu, Y.; Liu, J.; Elsworth, D.; Chen, Z.; Connell, L.; Pan, Z. Dual poroelastic response of a coal seam to CO_2 injection. *Int. J. Greenhouse Gas Control* **2010**, *4*, 668−678.

(9) Fan, C.; Elsworth, D.; Li, S.; Zhou, L.; Yang, Z.; Song, Y. Thermo-hydro-mechanical-chemical couplings controlling CH_4 production and CO_2 sequestration in enhanced coalbed methane recovery. *Energy* **2019**, *173*, 1054−1077.

(10) Gray, I. Reservoir engineering in coal seams: part 1-the physical process of gas storage and movement in coal seams. *SPE Reserv. Eng.* **1987**, *2*, 28−34.
(11) Seidle, J. P.; Jeansonne, M. W.; Erickson, D. J. *Application of Matchstick Geometry to Stress Dependent Permeability in Coals*, Proceedings of the SPE Rocky Mountain Regional Meeting; Casper, WY, May 18−21, 1992.
(12) Palmer, I.; Mansoori, J. *How Permeability Depends on Stress and Pore Pressure in Coalbeds: A New Model*, Annual Technical Conference and Exhibition, Denver, CO, Oct. 6−9, 1996, SPE 24361.
(13) Shi, J. Q.; Durucan, S. Drawdown induced changes in permeability of coalbeds: a new interpretation of the reservoir response to primary recovery. *Transport. Porous. Med.* **2004**, *56*, 1−16.
(14) Zhang, H.; Liu, J.; Elsworth, D. How sorption-induced matrix deformation affects gas flow in coal seams: a new FE model. *Int. J. Rock. Mech. Min.* **2008**, *45*, 1226−1236.
(15) Wu, Y.; Liu, J.; Chen, Z.; Elsworth, D.; Pone, D. A dual poroelastic model for CO2-enhanced coalbed methane recovery. *Int. J. Coal. Geol.* **2011**, *86*, 177−189.
(16) Wu, K.; Li, X.; Guo, C. et al. *Adsorbed Gas Surface Diffusion and Bulk Gas Transport in Nanopores of Shale Reservoirs with Real Gas Effect Adsorption-mechanical Coupling*, SPE Reservoir Simulation Symposium, Houston, TX, USA, Feb. 23−25, Society of Petroleum Engineers: Richardson, TX, USA, 2015, SPE 173201.
(17) Liu, T.; Lin, B.; Yang, W. Impact of matrix−fracture interactions on coal permeability: model development and analysis. *Fuel* **2017**, *207*, 522−532.
(18) Wang, G.; Xiao, Z.; Yu, J.; Zhang, L.; Sun, L. An improved coal permeability model with variable cleat width and Klinkenberg coefficient. *Geotech. Geol. Eng.* **2020**, *38*, 3041−3051.
(19) Jiang, C.; Zhao, Z.; Zhang, X.; Liu, J.; Elsworth, D.; Cui, G. Controlling effects of differential swelling index on evolution of coal permeability. *J. Rock. Mech. and Geotech.* **2020**, *12*, 461−472.
(20) Du, X.; Cheng, Y.; Liu, Z.; Yin, H.; Wu, T.; Huo, L.; Shu, C. CO_2 and CH_4 adsorption on different rank coals: A thermodynamics study of surface potential, Gibbs free energy change and entropy loss. *Fuel* **2021**, *283*, No. 118886.
(21) Wang, C.; Liu, R.; Jiang, Y.; Wang, G.; Luan, H. Effect of shear-induced contact area and aperture variations on nonlinear flow behaviors in fractal rock fractures *J. Rock. Mech. Geotech.* 2022, DOI: 10.1016/j.jrmge.2022.04.014.
(22) Liu, J.; Chen, Z.; Elsworth, D.; Qu, H.; Chen, D. Interactions of multiple processes during CBM extraction: a critical review. *Int. J. Coal. Geol.* **2011**, *87*, 175−189.
(23) Ma, T.; Rutqvist, J.; Oldenburg, C. M.; Liu, W. Coupled thermal−hydrological−mechanical modeling of CO_2-enhanced coalbed methane recovery. *Int. J. Coal. Geol.* **2017**, *179*, 81−91.
(24) Chen, Z.; Liu, J.; Pan, Z.; Connell, L. D.; Elsworth, D. Influence of the effective stress coefficient and sorption-induced strain on the evolution of coal permeability: model development and analysis. *Int. J. Greenhouse Gas Control* **2012**, *8*, 101−110.
(25) Liu, T.; Lin, B.; Yang, W.; Zhai, C.; Liu, T. Coal permeability evolution and gas migration under non-equilibrium state. *Transp. Porous Media* **2017**, *118*, 393−416.
(26) Peng, Y.; Liu, J.; Wei, M.; Pan, Z.; Connell, L. D. Why coal permeability changes under free swellings: New insights. *Int. J. Coal. Geol.* **2014**, *133*, 35−46.
(27) Wang, G.; Wang, K.; Wang, S.; Elsworth, D.; Jiang, Y. An improved permeability evolution model and its application in fractured sorbing media. *J. Nat. Gas. Sci. Eng.* **2018**, *56*, 222−232.
(28) Somerton, W. H.; Söylemezoğlu, I. M.; Dudley, R. C. Effect of stress on permeability of coal. *Int. J. Rock Mech. Min. Sci.* **1975**, *12*, 129−145.
(29) Cui, X.; Bustin, R. M. Volumetric strain associated with methane desorption and its impact on coalbed gas production from deep coal seams. *AAPG Bull.* **2005**, *89*, 1181−1202.
(30) Wei, M. Y.; Liu, J.; Liu, Y. K.; Liu, Z. H.; Elsworth, D. Effect of adsorption-induced matrix swelling on coal permeability evolution of micro-fracture with the real geometry. *Petrol Sci.* **2021**, *18*, 1143−1152.
(31) Kou, Z.; Zhang, D.; Chen, Z.; Xie, Y. Quantitatively determine CO_2 geosequestration capacity in depleted shale reservoir: A model considering viscous flow, diffusion, and adsorption. *Fuel* **2022**, *309*, No. 122191.
(32) Klinkenberg, L. J. The Permeability of Porous Media to Liquids and Gases. In *Drilling and Production Practice*, American Petroleum Institute: Washington, DC, 1941; pp 200−213.
(33) Civan, F.; Rai, C. S.; Sondergeld, C. H. Shale-gas permeability and diffusivity inferred by improved formulation of relevant retention and transport mechanisms. *Transp. Porous Media* **2011**, *86*, 925−944.
(34) Ashrafi Moghadam, A.; Chalaturnyk, R. Expansion of the Klinkenberg's slippage equation to low permeability porous media. *Int. J. Coal. Geol* **2014**, *123*, 2−9.
(35) Wang, Z.; Fink, R.; Wang, Y.; Amann-Hildenbrand, A.; Krooss, B. M.; Wang, M. Gas permeability calculation of tight rocks based on laboratory measurements with non-ideal gas slippage and poroelastic effects considered. *Int. J. Rock. Mech. Min.* **2018**, *112*, 16−24.
(36) Xiao, W.; Bernabé, Y.; Evans, B.; Mok, U.; Zhao, J.; Ren, X.; Chen, M. Klinkenberg effect and effective pressure for gas permeability of tight sandstones. *J. Geophys. Res.: Solid Earth* **2019**, *124*, 1412−1429.
(37) Chen, Y.; Jiang, C.; Leung, J. Y.; Wojtanowicz, A. K.; Zhang, D.; Zhong, C. Second-order correction of Klinkenberg equation and its experimental verification on gas shale with respect to anisotropic stress. *J. Nat. Gas. Sci. Eng.* **2021**, *89*, No. 103880.
(38) Zhou, L.; Feng, Q.; Chen, Z.; Liu, J. Modeling and upscaling of binary gas coal interactions in CO_2 enhanced coalbed methane recovery. *Procedia. Environ. Sci.* **2012**, *12*, 926−939.
(39) Fang, H.; Sang, S.; Liu, S. The coupling mechanism of the thermal-hydraulic-mechanical fields in CH_4-bearing coal and its application in the CO_2-enhanced coalbed methane recovery. *J. Petrol. Sci. Eng.* **2019**, *181*, No. 106177.
(40) Liu, J.; Wang, J.; Chen, Z.; Wang, S.; Elsworth, D.; Jiang, Y. Impact of transition from local swelling to macro swelling on the evolution of coal permeability. *Int. J. Coal. Geol.* **2011**, *88*, 31−40.
(41) Peng, Y.; Liu, J.; Pan, Z.; Connell, L. D.; Chen, Z.; Qu, H. Impact of coal matrix strains on the evolution of permeability. *Fuel* **2017**, *189*, 270−283.
(42) Wei, M.; Liu, J.; Elsworth, D.; Li, S.; Zhou, F. Influence of gas adsorption induced non-uniform deformation on the evolution of coal permeability. *Int. J. Rock. Mech. Min.* **2019**, *114*, 71−78.
(43) Zeng, J.; Liu, J.; Li, W.; Guo, J. A process-based coal swelling model: Bridging the gaps between localized swelling and bulk swelling. *Fuel* **2021**, *293*, No. 120360.
(44) Zhang, S.; Liu, J.; Wei, M.; Elsworth, D. Coal permeability maps under the influence of multiple coupled processes. *Int. J. Coal. Geol.* **2018**, *187*, 71−82.
(45) Langmuir, I. The adsorption of gases on plane surfaces of glass, mica and platinum. *J. Am. Chem. Soc.* **1918**, *40*, 1361−1403.
(46) Ren, T.; Wang, G.; Cheng, Y.; Qi, Q. Model development and simulation study of the feasibility of enhancing gas drainage efficiency through nitrogen injection. *Fuel* **2017**, *194*, 406−422.
(47) Liu, H. H.; Rutqvist, J. A new coal-permeability model: internal swelling stress and fracture−matrix interaction. *Transp. Porous Media* **2010**, *82*, 157−171.
(48) Mian, C.; Zhida, C. Effective stress laws for multi-porosity media. *Appl. Math. Mech.* **1999**, *20*, 1207−1213.
(49) Chen, Z.; Liu, J.; Elsworth, D.; Connell, L. D.; Pan, Z. Impact of CO_2 injection and differential deformation on CO_2 injectivity under in-situ stress conditions. *Int. J. Coal. Geol.* **2010**, *81*, 97−108.
(50) Wu, Y.; Liu, J.; Elsworth, D.; Miao, X.; Mao, X. Development of anisotropic permeability during coalbed methane production. *J. Nat. Gas. Sci. Eng.* **2010**, *2*, 197−210.
(51) Wang, L.; Wang, Z.; Li, K.; Chen, H. Comparison of enhanced coalbed methane recovery by pure N_2 and CO_2 injection: Experimental observations and numerical simulation. *J. Nat. Gas. Sci. Eng.* **2015**, *23*, 363−372.

(52) Wang, G.; Wang, K.; Jiang, Y.; Wang, S. Reservoir permeability evolution during the process of CO_2-enhanced coalbed methane recovery. *Energies* **2018**, *11*, 2996.
(53) Xia, T.; Zhou, F.; Liu, J.; Hu, S.; Liu, Y. A fully coupled coal deformation and compositional flow model for the control of the pre-mining coal seam gas extraction. *Int. J. Rock. Mech. and Min.* **2014**, *72*, 138−148.
(54) Vishal, V.; Singh, T. N.; Ranjith, P. G. Influence of sorption time in CO_2-ECBM process in Indian coals using coupled numerical simulation. *Fuel* **2015**, *139*, 51−58.
(55) Xu, H.; Tang, D. Z.; Tang, S. H.; Zhao, J. L.; Meng, Y. J.; Tao, S. A dynamic prediction model for gas−water effective permeability based on coalbed methane production data. *Int. J. Coal. Geol.* **2014**, *121*, 44−52.
(56) Leverett, M. Capillary behavior in porous solids. *Trans. AIME* **1941**, *142*, 152−169.
(57) Wong, S.; Law, D.; Deng, X.; Robinson, J.; Kadatz, B.; Gunter, W. D.; Zhiqiang, F.; et al. Enhanced coalbed methane and CO_2 storage in anthracitic coals-Micro-pilot test at South Qinshui, Shanxi, China. *Int. J. Greenhouse Gas Control* **2007**, *1*, 215−222.
(58) Chen, D.; Pan, Z.; Liu, J.; Connell, L. D. An improved relative permeability model for coal reservoirs. *Int. J. Coal. Geol.* **2013**, *109−110*, 45−57.

https://doi.org/10.1021/acsomega.2c03377
ACS Omega 2022, 7, 31167−31182